Multi-Parameter Optimized Triboelectric Nanogenerator Based Self-Powered Sensor Network for Broadband Aeolian Vibration Online-Monitoring of Transmission Lines

Han Wu, Jiyu Wang,* Zhiyi Wu, Shenglin Kang, Xuelian Wei, Hanqing Wang, Hao Luo, Lijun Yang, Ruijin Liao, and Zhong Lin Wang*

Overhead transmission lines are vulnerable to aeolian vibrations that threaten the operation of the power grid. A triboelectric nanogenerator (TENG) based self-powered system offers a desirable way for vibration online-monitoring with potential for large-scale deployment. In this work, a self-powered sensor network constructed by active vibration sensor (AVS) units with a spring-mass based TENG (S-TENG) is reported for effective energy harvesting and broadband vibration sensing. The basic TENG with structural parameters is first discussed from the aspects of efficiency and response characteristics, then the spring constant and mass weight are also adjusted for S-TENGs with different optimal operation regions, thus the overall vibration amplitude and frequency response are further enhanced by the mutual compensation of S-TENGs with a weight allocation strategy. Furthermore, the S-TENGs are combined with external circuits to compose the AVS units, which are deployed in a distributed manner on a simulated transmission line to demonstrate a self-powered wireless warning system and an aeolian vibration mapping system, enabling abnormal vibration warnings and vibration distribution monitoring over the whole line. This work represents a novel strategy for utilizing TENG technology for transmission line aeolian vibration monitoring and provides valuable guidance for further sensor network construction and power grid visualization.

1. Introduction

Electric Internet of Things (eIoT) has been tremendously evolved with the advance of IoT, which involves trillions of distributed sensors being installed at various nodes for online-monitoring the operation of the power grid.[1–4] The overhead transmission lines, regarded as the blood vessels in human body, play essential roles in energy transport and distribution as well as future "carbon emission reaching the peak and eventually carbon neutralization". On the demands of high-voltage delivery, the transmission lines are normally designed in extended span length and elevated height with wide cross-section, which are vulnerable to the aeolian vibration produced by Von Karman vortex.[5–6] This phenomenon will push the line into an up-and-down motion in vertical direction, causing fatigues, broken strands, even broken wires in transmission lines, seriously threatening the safety and reliability of power grid.[7–9] Thus, the aeolian vibration sensors are necessarily provided to monitor the state of transmission lines through the vibration amplitude and frequency. The fiber-optic and the piezoelectric-based sensors as the most common aeolian vibrations sensors have been applied for online-monitoring with unignorable limitations.[10–14]

The major result deviations caused by the slight fluctuation of the light source as well as the high cost of fiber optic material restrict the further large-scale installation of the fiber-optic sensors. And the piezoelectric-based ones are also troubled with the serious nonlinear relational errors between the material

H. Wu, J. Wang, S. Kang, H. Wang, H. Luo, L. Yang, R. Liao
State Key Laboratory of Power Transmission Equipment and System
Security and New Technology
Chongqing University
Shapingba, Chongqing 400044, P. R. China
E-mail: jiyuwang@cqu.edu.cn

J. Wang
Tsinghua-Berkeley Shenzhen Institute
Tsinghua Shenzhen International Graduate School
Tsinghua University
Shenzhen 518055, P. R. China

Z. Wu, X. Wei, Z. L. Wang
Beijing Institute of Nanoenergy and Nanosystems
Chinese Academy of Sciences
Beijing 100083, P. R. China
E-mail: zlwang@binn.cas.cn

Z. L. Wang
CUSPEA Institute of Technology
Wenzhou, Zhejiang 325024, P. R. China

Z. L. Wang
School of Material Science and Engineering
Georgia Institute of Technology
Atlanta, GA 30332, United States

ADVANCED
SCIENCE NEWS

www.advancedsciencenews.com

ADVANCED
ENERGY
MATERIALS

www.advenergymat.de

deformation and actual vibration.[15,16] Meanwhile, such sensors are still battery-based devices, hence the tough issues like a limited lifetime, risk of environmental pollution, and low device maintainability should be addressed especially in large-scale deployment. In addition, the typical coil-based energy harvesters based on electromagnetic induction cannot be operated in the DC power line, which has been the main trend of the power grid development, and there are still drawbacks in AC lines such as the extremely dependent on the line condition, and the hardly eliminated remnant magnetism leading to the overheating concerns and performance degradation. The emergence of triboelectric nanogenerator (TENG) opens up a new pathway for the state-sensing field.[17–19] As driven by Maxwell's displacement current, the TENG on one hand can harvest various types of ambient mechanical energy into electric power to ensure the distributed energy supply, and linearly perceives the surrounding mechanical excitation, such as vibrations and accelerations.[20–22] With the merits of low cost, flexible structure, and diverse materials, the TENGs can be further developed into a self-powered active sensor, which renders itself to be a practical and effective strategy to lay the foundation for the development and expansion of eIoT.

Previously, TENG-based vibration sensors have been designed mostly in two main modes (i.e., sliding mode and contact separation mode). The sliding mode is designed to shift the slider relative to the two horizontal stator electrodes for reflecting vibrations.[23–25] However, the contact surfaces between the slider and the stators need to be kept in close and rigid contact, making the material surfaces vulnerable to abrasion with less durability, thus the standard value of the sensor signal will be distorted in the long-term operation. The contact separation mode of TENG (CS-TENG)[26–28] is a useful option for reassuring the above concerns, in which the electrification effect occurs in vertical direction only. However, since the vibrations of the transmission line are mainly presented in low-amplitude features, it is difficult for the triboelectric layers to fully contact with each other in the most CS-TENG prototypes, which limits the capability of efficient energy harvesting under such micro-vibrations and reliability of power supply for the auxiliary components (i.e., electronics, microcontroller unit (MCU), wireless module, etc.) in the self-powered system. An alternative way for improving the energy harvesting efficiency under the narrow amplitude space with the fixed device size is to enhance the longitudinal contact area by substituting the single-layered structure with the multi-stack layered structure. Such a 3D multi-layer structure not only enables high power density, but also offers favorable structural optimization and buffering function to satisfy the practical requirements to a great extent.[29,30]

Besides the issues of power supply, the state-awareness performance of TENG as the sensor device should also be concerned. Generally, a designed TENG even with well-optimized structural parameters can only operate in a specific response spectrum, whose perception might decrease in the entirely different vibrations when exposed to the complex transmission line environment. For example, a TENG designed in the low amplitude response will soon output saturatedly as the intensity increase, while a TENG with the opposite feature cannot recognize the weak excitation, even affect the energy conver-

sion, with plenty of vibrations energy failing to be collected. Inspired by the typical spring-mass system, the idea of utilizing TENG to be integrated with the spring-based mechanical amplifier can be an effective and feasible way to achieve the flexible and broadband vibration response strategy.[31] This novel integration enables the ability to amplify the vibration states from slight excitation, and restrains the strong oscillation with unsaturated output through the reasonable and simple parameter adjustment. In this way, the TENG is able to achieve a superior sensing capability with no conflict of the optimum output performance through a customized choice of parameter settings of the spring-mass system, especially in the long-distance transmission lines with various vibrations regions.[32,33] More importantly, the integrated TENG can be further grouped into a network with several types of customized units operated perfectly in their own vibration regions, which can largely improve the measurement accuracy and the response characteristic. Furthermore, the credibility weights for each individual in the network should be analyzed based upon its own response property, and a detailed strategy for the weight alteration should be accordingly proposed. In this regard, even one unit fails in operation, the weight alteration strategy still ensures the overall result being immune to the data exceptions.

Herein, a multi-parameter optimized self-powered sensor network is proposed with a single active vibration sensor (AVS) unit composed of a spring-mass (S-) based TENG for the online vibration monitoring of transmission lines. The TENG is in a helical shape, and is designed into a 3D multi-layered structure instead of the typical single layer for effectively improving the efficiency by enhancing the longitudinal triboelectric layer area. Each helical layer is operated in the contact separation mode and driven by a spring-mass combination to enable itself as an energy harvester and a vibration sensor. For the basic TENG, its influential factors on the vibration sensing characteristics including the vibration space, helical layer numbers, and dielectric materials were systematically discussed for achieving a high sensitivity under a broad amplitude response. As an energy harvester, a maximum power of 2.5 mW can be provided from TENG, which is capable of driving the entire system. Moreover, the TENG is further integrated with a spring-mass combination for the purpose of adjustable response characteristics, through which the frequency and amplitude response property of the highly combined S-TENG was investigated and well-customized according to the various vibration regions, thus the frequency and amplitude response are significantly broadened when several S-TENGs are operated together with a reliable weight allocation strategy. Furthermore, the AVS device was developed based on the S-TENG with external electronic circuit modules (including signal processing circuit, MCU, Bluetooth module, etc.) assembled together, which demonstrates a self-powered wireless warning system for abnormal vibration state warnings. An array of AVS units distributively deployed on the transmission line demonstrates a transmission line aeolian vibration mapping system for the whole line vibration distribution monitoring. This proposed work can be utilized as an energy harvester for the micro-vibrations, and an aeolian vibration condition evaluation for the prevention of broken strands in transmission lines. It also offers a new concept and strategy

**ADVANCED
SCIENCE NEWS**
www.advancedsciencenews.com

**ADVANCED
ENERGY
MATERIALS**
www.advenergymat.de

that utilizes TENG as a single unit to be further grouped into a network system with more accurate, global, and reliable state-awareness application.

2. Results and Discussion

2.1. Structure and Working Mechanism of the TENG

Figure 1a demonstrates the self-powered sensor network for the aeolian vibration monitoring of the overhead transmission line. The network is composed of an array of AVS units cooperatively monitoring the overall line vibration state. The basic AVS unit is consists of two parts: a spring-mass based TENG (S-TENG) and an external circuit, in which the S-TENG can be further regarded as an integration of the TENG and the spring-mass combination system, as illustrated in Figure 1b. The TENG is designed into a 6-layered helical structure with an acrylic backbone and operates in the contact-separation mode. The Cu foil is attached on the front and back sides of the helical layer as the electrodes, and the polytetrafluoroethylene (PTFE) films entirely cover the front sides of the Cu electrodes to serve as the triboelectric layers, with the enlarged structural view in Figure 1b. The sponge is employed as a buffer installed between the electrode and acrylic layer for the soft contact and stability. With such a structure, the PTFE film in each layer can easily get fully in contact with the upper Cu electrodes alternately under micro-vibrations. In addition, the surfaces of the PTFE films were modified through the plasma-etching method to enhance the surface roughness, scanning electron microscopy (SEM) image of which is shown at the bottom right in Figure 1b. Moreover, the TENG is integrated with a combination of a spring and a mass block, which acts as an amplifier in response to any external vibration excitations and drives the TENG in a modulated way. As the connection part, the acrylic shaft is placed in the center and passes through the mass block, further ensuring the stability of the device in vertical vibrations. All of the above components are enclosed with an acrylic shell. Figure 1c,d depicts the photographs of the original TENG and the spring-mass-based TENG (S-TENG) integration, the S-TENG owns the dimensions of 80 mm × 80 mm × 70 mm (length × width × height). (The fabrication process is described with detail in the Experimental Section).

The working mechanism of the TENG is illustrated in **Figure 2**a. With any external vibration excitations, an alternative contact-separation movement forms between the layers of the TENG, and the electricity generation process accordingly occurs based on a coupled effect of triboelectrification and electrostatic induction. i) At the initial stage, the external excitation makes the PTFE film and the upper Cu electrode fully contact, creating an equal amount of negative and positive charges on their surfaces, respectively. As the excitation sustains, the PTFE
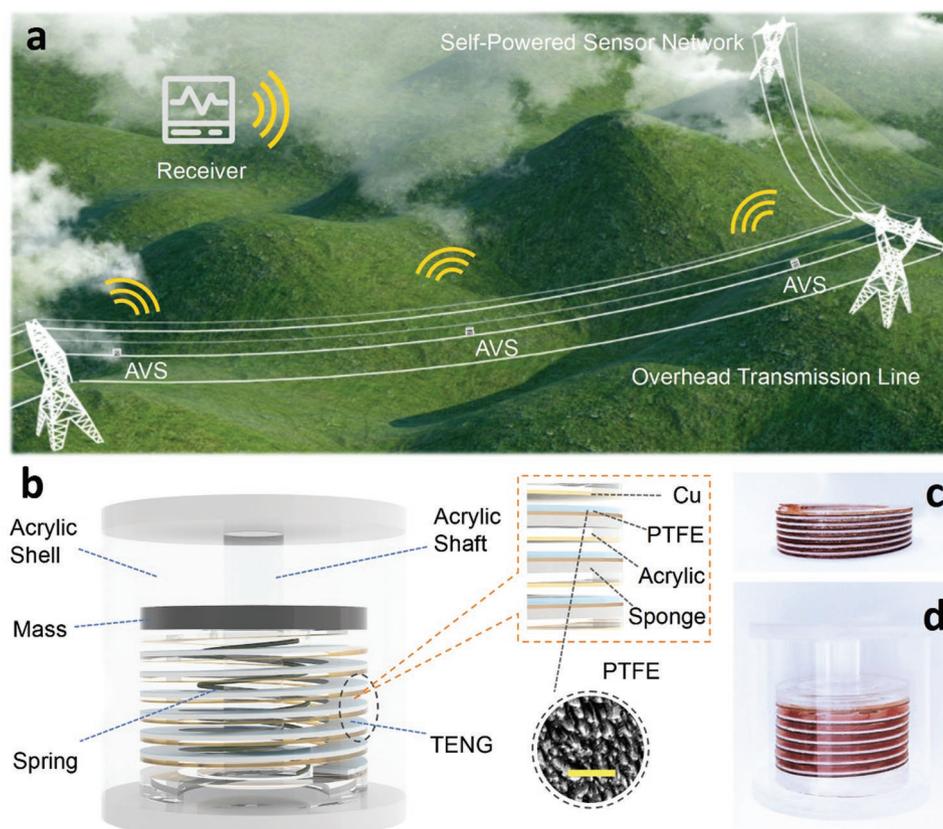
Figure 1. Structural design of the AVS-based self-powered sensor network. a) Schematic illustration of the aeolian vibration online-monitoring network based on the AVS units for the overhead transmission line. b) Structural composition of the S-TENG, scale bar in the SEM image is 1 μm. Photographs of c) the fabricated original TENG, and d) S-TENG.
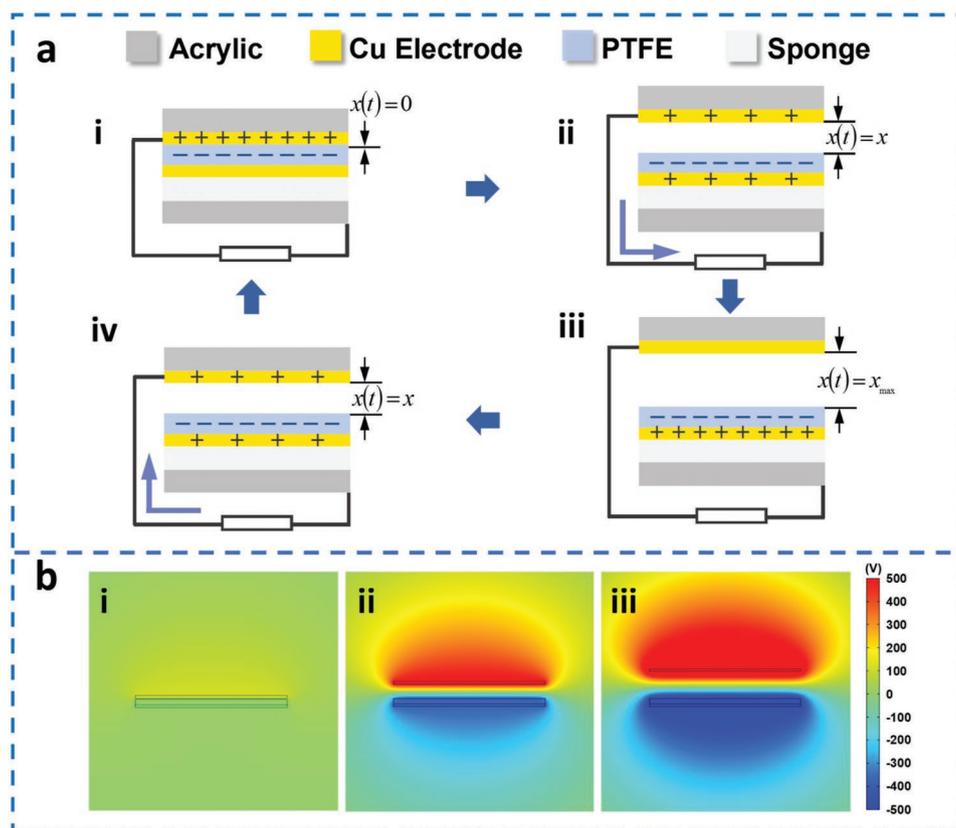
Figure 2. Schematics of the working mechanism of TENG. a) i–iv) Schematic of charge distribution and current direction in a cycle for a simplified TENG. b) i–iii) Finite element simulations exhibit the electric potential distribution under three typical stages via COMSOL.

film and the upper Cu electrode will separate start from $x = 0$. ii) Consequently, the original electrostatic balance breaks since the negative charges cannot be screened entirely, thus a potential difference between the electrodes establishes, causing the positive charges of the original electrode to transfer to another electrode through the external load to rebalance the electrostatic status. iii) This charge transfer continues until the separation is up to $x = x_{max}$, where the negative charges of PTFE film are totally screened by the positive ones from another electrode only. iv) After that, as the PTFE film moves back to the original position, the positive charges accordingly flow back to the upper Cu electrode to compensate the electrical potential differences, until the initial electrostatic balance establishes again. This is a full cycle of the electricity generation process for the TENG.

Furthermore, the charge distribution in the open circuit condition is also simulated and illustrated at three typical positions via COMSOL, as visualized in Figure 2b. The V_{oc} is defined as the electric potential difference between the two electrodes. The electrostatic induction process can generate the V_{oc} signal as the non-mobile negative triboelectric charges on PTFE film orderly screened by the positive triboelectric charges on Cu electrode. i) Therefore, in the initial contact stage, there is practically no potential difference since the two opposite charges with the same amount are offset with each other, and the V_{oc} at this time tends to be the minimum value. ii) The V_{oc} then increases as the potential difference establishes by the separation, and iii) reaches to the peak value at the maximum separation

distance. The variable V_{oc} can be analytically expressed by the Gauss' law, as shown below:[34]

$$V_{oc} = \frac{\sigma x(t)}{\varepsilon_0}, \ x \in [0, x_{max}] \tag{1}$$

where, x is the surface distance between the PTFE film and the Cu electrode, x_{max} is the maximum distance of the separation, σ is the surface triboelectric charge density of the PTFE film, and ε_0 is the dielectric constant of vacuum. With the given values of the above parameters, the theoretical maximum value of the V_{oc} is calculated as almost 1 kV, which is accorded with the simulation value.

2.2. Output Performance of the TENG

To characterize the electrical output performance of the TENG, a vibration electromagnetic shaker system with controllable frequency and amplitude is employed to simulate the vibration energy. The measurements were performed under different frequencies with a fixed amplitude of 5 mm, and the results present the open-circuit voltage (V_{oc}), short circuit current (I_{sc}), and transferred charge (Q_{sc}) of the TENG at typical frequencies in **Figure 3**a–c. Both V_{oc} and Q_{sc} rise rapidly with the frequency increased from 2 to 15 Hz, then drop gradually as the frequency continuously increases to 25 Hz. The V_{oc} and the Q_{sc} are

**ADVANCED
SCIENCE NEWS**

www.advancedsciencenews.com

**ADVANCED
ENERGY
MATERIALS**

www.advenergymat.de
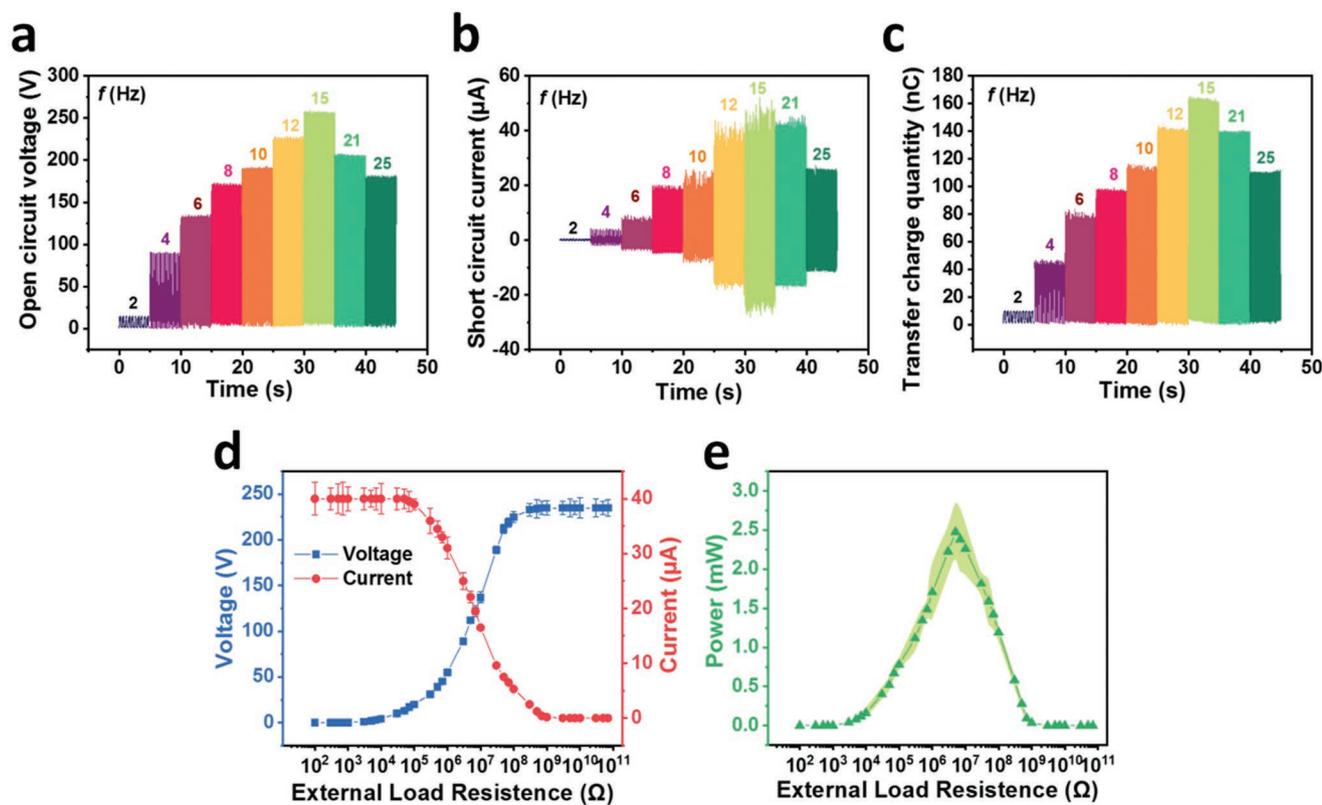
Figure 3. The electrical output performance of the TENG. a) open-circuit voltage (V_{oc}), b) short-circuit current (I_{sc}), and c) transfer charge quantity (Q_{sc}) of the TENG under several vibration frequencies controlled by a shaker. d) Variation of the output voltage, current, and e) peak power of the TENG depend on varied external load resistances. (The electrical values are obtained when the vibration amplitude is 5 mm).

maximized at the vibration frequency of 15 Hz with the values of 257 V and 165 nC, respectively. The reason for the maximum value at 15 Hz can be attributed to the resonant frequency of the current device, at which the separation distance reaches to the maximum value, thus exerting the greatest impact on the triboelectrification effect of the TENG. When a voltage signal is selected as the sensing signal, the sensor enables high sensitivity features to sense the vibration excitation, even at a vibration frequency of 2 Hz but still with voltage values of 15 V. It is noteworthy that the value difference between the actual voltage and theoretical one is a common phenomenon in the contact-separation operation mode, which can be attributed to the parasitic capacitances in the open-circuit loop.[35,36] The peak value of I_{sc} follows an upward trend with the frequency, and rises to the maximum value of 46 µA at a high growth rate before 15 Hz. The output current can be defined as the flow rate of the charges, thus the increased frequency largely enhances the flow rate of the charges, resulting in the swift ascent of the I_{sc} before the peak value, while the I_{sc} tends to decrease gradually after 15 Hz due to the reduction of the triboelectric charges by the reason of insufficient contact at such transient process. Once an external load is applied, the output voltage rises gradually with the increased load resistance, while the output current exhibits a reverse trend, as shown in Figure 3d,e. As a result, the instantaneous output power of the TENG is maximized at a load resistance of ≈5 MΩ, corresponding to a peak power value of ≈2.5 mW.

2.3. Structural Parameters Optimization of the TENG

The performance of the TENG in terms of the energy supply as well as perception sensor is mainly influenced by the structural parameters, such as the overall vibration space, the helical layer numbers, and the surface charge density within the triboelectric materials, which should be studied respectively. As shown in **Figure 4**a, the TENGs were first designed into different overall vibration spaces of 25, 30, and 35 mm, which relevant setting rules as shown in Note S1, Supporting Information, and the relationships between the voltage signal V_{oc} and the vibration amplitude z_0 in the range of 0.2–5 mm are collected under a fixed frequency (12 Hz) in Figure S1, Supporting Information, and the linear fitting was applied for a better comparison on the response performance, with the results plotted in Figure 4b. For the 25 mm, the V_{oc} increases linearly with the vibration amplitude in the low amplitude area (0.2–3 mm), but it becomes saturated over the further increment of amplitude. This is because the compressed vibration space will have an adverse effect on the vibrations, particularly in the high amplitude range. In the 35 mm situation, such a saturation is not observed in the high amplitude range, but the initial point for the linear fitting curve occurs at a high amplitude of 1.5 mm, which can be considered as the reason that the contact-separation mode is hardly triggered under low amplitude with the larger vibration space. While for the fitting curve of 30 mm, the curve exhibits a favorable linear degree under the whole vibration amplitude
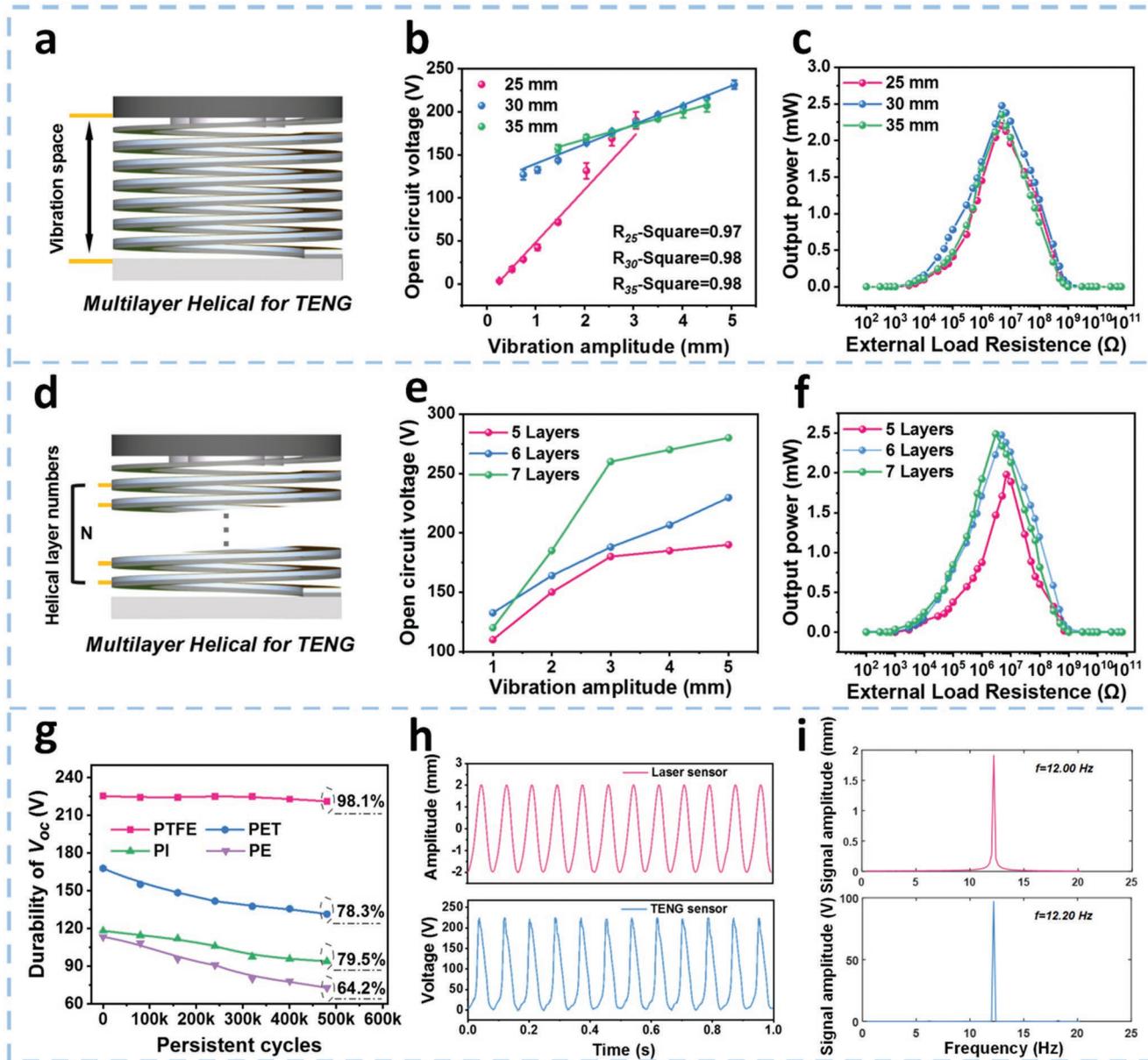
Figure 4. Structural parameters optimization of the TENG. a) Schematic illustration of the TENG in various vibration spaces, with the corresponding b) voltage signal V_{oc} and the vibration amplitude z_0 relationship, and c) output peak powers curve under varied external load resistances. d) Schematic illustration of the TENG in various helical layer numbers, with the corresponding e) voltage signal V_{oc} and the vibration amplitude z_0 relationship, and f) output peak powers curve under varied external load resistances. g) Durability of V_{oc} values for the TENG fabricated with different triboelectric materials. h) Vibration amplitude signal captured by commercial laser sensor and voltage signal captured by TENG, and i) the corresponding frequency spectrum calculated by the fast Fourier transform.

range of 0.7–5 mm with a satisfactory goodness, which should be considered as the designed vibration space value. Meanwhile, the outputs for the three sets of TENGs were also investigated with a series of load resistances in the varied vibration spaces (Figure 4c, Figure S2, Supporting Information), in which the vibration space of 30 mm shows a maximum output power of 2.5 mW. In this regard, the output power is improved by a 13.6% compared to the original vibration space.

Under the determined vibration space of 30 mm, the TENG was fabricated into several helical structures with different

numbers of layers, and the output characteristics were also systematically measured by a series of the varied vibration amplitudes in Figure 4d. The relationships between the voltage signal V_{oc} and the vibration amplitude z_0 in the range of 1–5 mm are shown in Figure 4e. Generally, the V_{oc} for three sets of TENG tends to rise with z_0, which is attributed to the larger separation between the layers at the increased vibration amplitude z_0. Specifically, for the 5-layered TENG, the relationship between V_{oc} and z_0 can be divided into two sections, in which the V_{oc} increases linearly with z_0 growing from 1 to 3 mm, and reaches

**ADVANCED
SCIENCE NEWS**
www.advancedsciencenews.com

**ADVANCED
ENERGY
MATERIALS**
www.advenergymat.de

to the saturation status over 3 mm vibration amplitude. Similarly, the V_{oc} of the 7-layered TENG also has a saturation tendency when the vibration amplitude exceeds 3 mm. However, the 6-layered TENG differs from the others in the upward trend, the V_{oc} linearly grows up to 237 V when the vibration amplitude increased from 1 to 5 mm. The reason for the different trends can be attributed to the working mechanism of the CS-TENG. As for any kind of CS-TENGs, there is an optimum separation distance where the negative charges of triboelectric layer are fully screened by the opposite charges from only one electrode. Therefore, the practical distance that is less than the optimum separation will cause the reduction of the V_{oc}, and any further separations that exceed the optimum distance will not promote the V_{oc}.[35] It can be concluded that the average separation distance in 6-layered TENG is close to the optimum separation value, thus the average distance in 5-layered exceeds and that in 7-layered is inferior to the optimum one, rendering the 6-layered a better linearity. Meanwhile, the typical voltage and current outputs of the three TENGs are measured through the external load resistances (Figure S3, Supporting Information), and the obtained output power is plotted in Figure 4f. With the increasing number of layers, the peak value of the output power increases dramatically from 1.9 to 2.5 mW, then gradually to 2.6 mW, while the matched resistance value gradually becomes smaller. It can be calculated that the peak output power of the optimum 6-layered TENG is improved by 31.5% compared to the unoptimized one.

Furthermore, the effects of dielectric materials on both output and durability for the TENG were also compared. The traditional triboelectric materials like polyethylene (PE), polyimide (PI), polyethylene terephthalate (PET), and PTFE were applied in the TENG with the same thickness of 100 μm. As the TENG continuously be triggered by the vibrational excitation with a 2 mm amplitude and 12 Hz frequency, the comparison of the output and durability through the V_{oc} values for different materials are shown in Figure 4g (and the I_{sc} values are shown in Figure S4, Supporting Information). The values of V_{oc} for those materials reflect their ability to generate triboelectric charges, which is accorded with the electronegativity sequence.[37,38] In particular, the PTFE exhibits the most electron affinity with a maximum value of 225 V. On the other hand, the values of V_{oc} over the long testing cycles can reflect the durability, while the V_{oc} values of PE, PI, PET, and PTFE are degraded by 35.8%, 20.5%, 21.7%, and 1.9%, over 500k cycles operation respectively. The above results indicate the PTFE is an effective and stable triboelectric material for the TENG fabrication, and the TENG with contact-separation mode operates in a way of minimal friction and abrasion on both triboelectric layer surfaces, which also largely enhances the stability for the long-term operation.

Figure 4h shows the comparison result between the signals detected by the TENG and the commercial laser sensor. Under a periodic vibration excitation by the shaker (2 mm amplitude and 12 Hz frequency), the signal captured from the TENG is a high output sinusoidal waveform, which is well matched to the signal from the laser sensor. Meanwhile, derived from the signal of the TENG, the vibration frequency can be obtained via fast Fourier transform, and the calculated frequency also corresponds to that of the laser sensor in Figure 4i. This favorable feedback signal sustains the excellent sensing capability of the TENG as a vibration detection sensor.

2.4. Integration of the Spring-Mass Combination

Even with the optimized structural parameters, the TENG still cannot sustain the excellent response characteristics under the varied vibrations in view of the complicated environments that the overhead transmission line passes through. In this regard, a flexible and broadband vibration response strategy is proposed, in which the TENG is further integrated with an independent spring-mass combination. As shown in **Figure 5**a, the bottom of the TENG is fixed to a base and the top is attached to the moveable mass block to compose a spring-mass-based TENG (S-TENG) integration. The coordinated motions of the spring and mass block can be modeled as a single-degree-of-freedom second-order spring-mass system.[39] According to the force analysis, the differential equation for the relative motion $x(t)$ of the mass block with respect to the vibration excitation $z(t)$ is:

$$m\frac{d^2(z(t)+x(t))}{dt^2} + p\frac{dx(t)}{dt} + kx(t) = 0 \tag{2}$$

where, m is the mass weight, p is the damping constant, and k is the spring constant. For a sine excitation vibration track, $z = z_0\sin(\omega t)$, the motion amplitude (x_0) of the mass block can be expressed as follows:

$$x_0 = \frac{z_0\beta^2}{\sqrt{[1-\beta^2]^2 + 4\zeta^2\beta^2}} \tag{3}$$

where, β is the ratio of the vibration frequency (ω) to the resonant frequency (ω_0). ζ is the damping factor. Thus, the excitation response is caused by the relative movement of the movable mass block and bottom base. As a result, S-TENG can be driven by the excitation in a flexible response with the tunable spring-mass combination. (Detailed excitation responses are given in Note S2, Supporting Information).

Figure 5b illustrates the frequency response of the S-TENG (187 N m^{-1} spring constant, 30.5 g mass weight), the excitation holds a fixed amplitude of 2 mm with the frequency regulated from 1 to 50 Hz at an increasing step of 1 Hz. The peak value of V_{oc} for the S-TENG is maximized at the resonant frequency of 12 Hz, then decreases slowly after the resonant frequency. Theoretically, the resonant frequency of the S-TENG is given as follows:

$$f_0 = \frac{\omega_0}{2\pi} = \frac{1}{2\pi}\sqrt{\frac{k}{m}} \tag{4}$$

where the spring constant k and the mass weight m both influence the frequency response of the S-TENG. Based on Equations (3) and (4), the relative movement between the mass block and the bottom base of the S-TENG can be calculated. (Detailed procedure in Note S3, Supporting Information). It can be discovered that the higher output can be attributed to the larger relative displacement of the S-TENG. Figure 5c, d further discovers the frequency response of the S-TENG influenced by
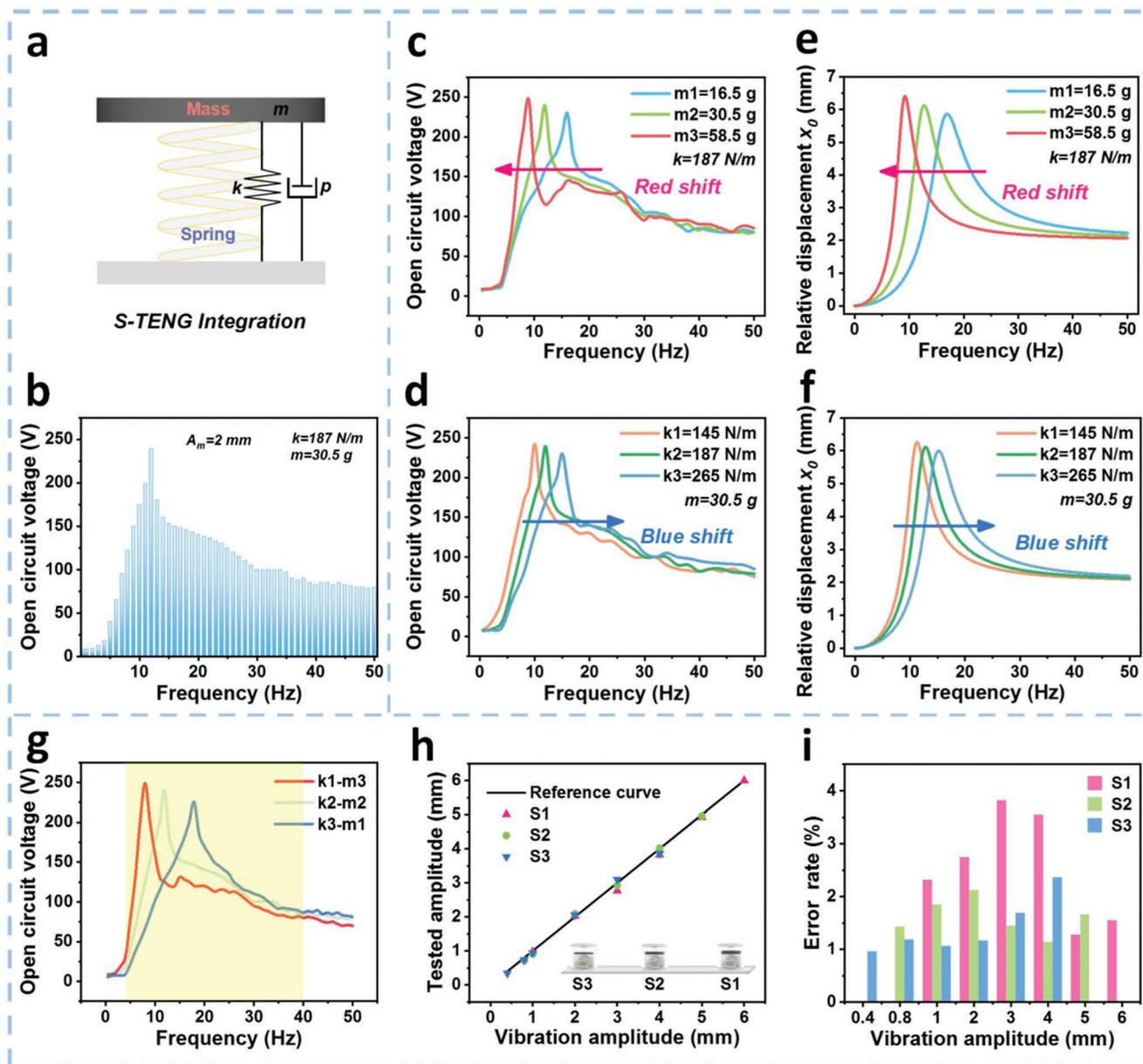
Figure 5. Parameters adjustment of the spring-mass combination system for the S-TENG integration. a) Schematic illustration of the S-TENG integration. b) Measured frequency response of the S-TENG, and their frequency response curves when varying c) mass weight and d) spring constant. Simulated frequency response curves of the S-TENG when varying e) mass weight and f) spring constant. g) Frequency response overlap region of the three typical S-TENGs. h) The linear relationship and i) error rates between the actual amplitude and the test amplitude calculated from the selected S-TENGs.

various spring constants and masses. It can be seen that the applied mass block increased from 16.5 to 58.5 g causes a red-shift in the output response curves, which results in a lower resonant frequency signal with higher output. Notably, although a mass is introduced to regulate the frequency response, the overall weight of the sensor will not exceed 200 g, which is much lighter than the conventional electromagnetic coils-based sensors. In contrast, a larger spring constant tends toward a higher resonant frequency with a lower output signal, and the response curve presents a blue shift. The frequency response characteristics are also simulated based on the above experimental variables with the results shown in Figure 5e,f, in which

the curves' translation is consistent with the experimental results. Thus, it is concluded that the variable parameters m and k enable the S-TENG to have a tunable frequency response. In addition, a further calculation of the resonant frequency regularity affected by the spring constant and the mass weight is provided in Figure S5, Supporting Information, which can be used as a guide for the configuration of the frequency response of the device.

Furthermore, three typical S-TENGs (S1, S2, and S3) with the tunable parameters matches with $k1$-$m3$, $k2$-$m2$, and $k3$-$m1$, respectively, were configured into different frequency response regions, as depicted in Figure 5g. Once the S-TENGs are

ADVANCED
SCIENCE NEWS
www.advancedsciencenews.com

ADVANCED
ENERGY
MATERIALS
www.advenergymat.de

assembled together, their frequency response regions will overlap with each other, enabling a broad frequency response region of 5–50 Hz. Notably, these S-TENGs exhibit different signal outputs as their responses under the same excitation due to the response degree. As for the amplitude response, the relationship between the vibration amplitude and V_{oc} signal of the three sensors were tested and the corresponding linear fitting curves were calculated respectively, under a fixed frequency of 20 Hz, in Figure S6, Supporting Information. It can be seen that the signal output for the S3 has been enhanced, while that for the S1 has been suppressed compared with the normal signal of the S2. Through the established fitting curves, the test amplitude of the output signal can be calculated, and Figure 5h displays the relationship between the test amplitude and the actual one for these TENGs. It can be observed that the measured values of the three S-TENGs are well accorded with the actual values under their individual effective measurement ranges. The S1 can be used for the larger amplitude measurement with the maximum value of 6 mm, while the minimum amplitude (0.4 mm) can be detected by the S3. The reason for the different amplitude responses is that the S1 with a resonant frequency of 8 Hz is far away from the test frequency, which results in a slighter response behavior that delays the occurrence of saturation vibration distance to a larger amplitude. While the resonant frequency for the S3 is 18 Hz, which operates nearly at the optimum vibration status that can produce a higher signal at a small amplitude but saturates under the amplitude of 4 mm.

The measurement errors of the S-TENGs were also investigated by a comparison between the test amplitude and the actual amplitude. The calculation equation of the error rate e_i can be defined as:

$$e_i = \frac{|A_{m.i} - A_{m.S}|}{A_{m.X}} \times 100\% \tag{5}$$

where $A_{m.i}$ is the test amplitude measured by the S-TENG, $A_{m.S}$ is the actual amplitude generated by the shaker, and $A_{m.X}$ is the measurable amplitude range of the S-TENG. Hence the error rate for the three S-TENGs at various amplitudes can be calculated, with the results shown in Figure 5i. The maximum error rates of S1, S2, and S3 are limited to 3.7%, 2.1%, and 2.3%, respectively. Specifically, the S1 exhibits a better accuracy with a wider amplitude region, whose error rate is less than 1.5%. While the S3 is more suitable to be adapted in the low amplitude region, with an error rate that less than is 1.1%. Such results are attributed to the response degrees of the devices as above mentioned.

In view of the different amplitude response features of these S-TENGs, the results will be more credible by superposing the measured data from individuals with particular assigned weights, which also promote the overall monitor performance by integrating the complementary output characteristics of the S-TENGs. In this way, the test value obtained from each S-TENG can be recalculated by their assigned weights, and a reconstructed value $A_{m.re}$ can be obtained, which can be expressed as:

$$A_{m.re} = \sum_{i=1}^{n} w_i A_{m.i} \tag{6}$$

where w is the weight factor. The weight allocation strategy is based on the entropy weighting method, in which the indexes will be evaluated in terms of the error rate, that is, following the rule that smaller error rates account for heavier weight factors. As a result, the weight factors can be calculated as follows:

$$w_i = \frac{(1-e_i)}{\sum_{i=1}^{n}(1-e_i)} \tag{7}$$

Based on Equation (7), the specific weighting factors for the selected S-TENGs under different amplitudes are calculated, as detailed in Table S1, Supporting Information. Thus, the three S-TENGs with different response features can be further integrated to compose a network. Once a vibration excitation occurs, three S-TENGs in the network will work simultaneously to measure the amplitude, and the current amplitude value $A_{m.re}$ is determined by the weighted sum offered by each S-TENG. This proposed strategy enables the network to operate in a more credible and accurate way for vibration monitoring. Moreover, a feasible weight alteration strategy can also be introduced to enhance the reliability of the state-awareness. Once one or two of the S-TENGs breaks down or the data-packet dropout happens, weight alteration strategy initiates by setting corresponding weights to zero, and the others' weights will be readjusted based on their error rates, sustaining the results in an accepted fluctuation. In addition, from the results of weight assignment, it can be considered that the S3 with a high weight in the amplitude range of 0.4–2 mm is more suitable to adapt to the low amplitude region, while the S1 is obviously dominated in the amplitude range of 4–6 mm for effective high amplitude monitoring. Based on such features, these S-TENGs can be installed strategically at different positions to match the different vibration levels of the transmission line.

2.5. AVS Network Construction and Demonstration

The typical aeolian vibration distribution intervals of the overhead transmission line are illustrated in **Figure 6**a, in which the vibration intensity is greater at the center of the wire and slighter at the two ends near the anchoring towers.[40,41] Therefore, three vibration areas are defined according to the different intensities for the transmission line noted in Figure 6a. For practical application, the S-TENG is further integrated with the external circuits to construct a self-powered AVS unit. The external circuits have two main parts as shown in Figure 6b, the power supply part and the signal sensor part. For the power supply, the TENG works as an energy conversion device to harvest the vibration energy to convert into electricity, with the output flowing through a rectifier and being stored in a capacitor. The stored energy can be supplied as needed to serve the signal sensor part by a voltage regulator. The signal sensor function can be achieved by a series of signal processing modules such as a signal conditioner, an MCU module, and a Bluetooth module. The perceived electric signals generated by different vibrations will be filtered and converted into digital signals through the analog-to-digital converter (ADC), then these data will be compared with the preset threshold value in the MCU module to evaluate the necessity for the warning, which will be transmitted
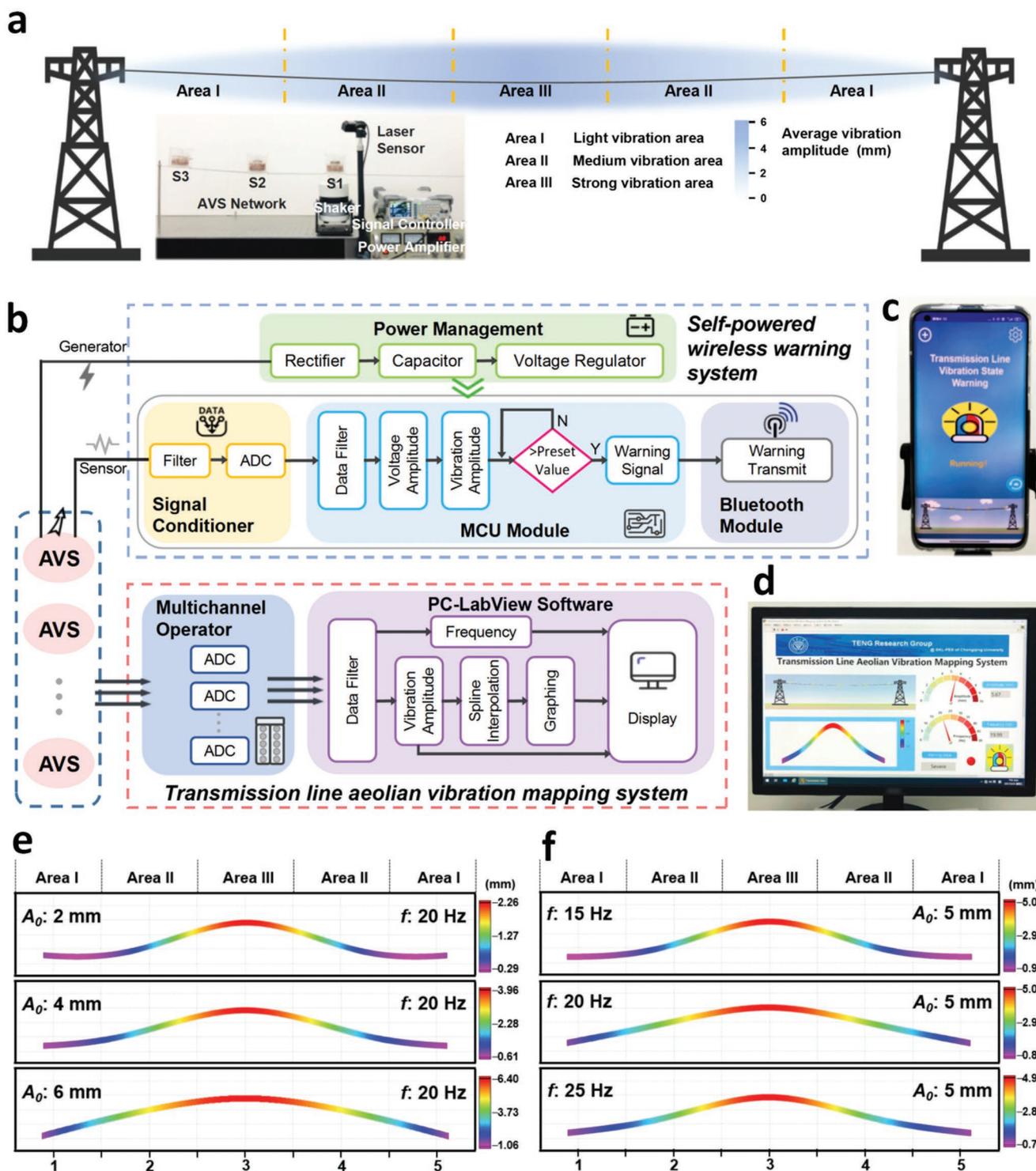
Figure 6. Demonstration of the AVS network for overhead transmission line aeolian vibration monitoring. a) Schematic illustration of the aeolian vibration distribution areas on the overhead transmission line. b) The work flow diagram of a self-powered wireless warning system with one single AVS unit, and a transmission line aeolian vibration mapping system based on the AVS network. c) Photograph of the vibration warning software to the mobile phones. d) Photograph of the vibration mapping system visual platform software with the AVS network. Demonstration of transmission line vibration mapping under e) various amplitudes and f) various frequencies.

via the Bluetooth module to the mobile phone. In this paper, a printed circuit board (PCB) on-board antenna is employed in the Bluetooth module, which can achieve a distance of 100 m

for stable data transmission. Also, an external antenna inlaid on the PCB board is optional for the distance enhancement (300–500 m). The constructed AVS units can be flexibly selected

ADVANCED
SCIENCE NEWS
www.advancedsciencenews.com

ADVANCED
ENERGY
MATERIALS
www.advenergymat.de

for different vibration areas as needed to form a self-powered sensor network. In our demonstration, a complete transmission line vibration monitoring platform is therefore established by an array of AVS units, where the S1, S2, S3 are installed for strong amplitude, medium amplitude, and light amplitude areas of the wire, respectively (Figure 6a, inset). An electromagnetic shaker is operated as an excitation source to simulate the aeolian vibration on the wire. The vibration amplitude and frequency can be regulated via signals programmer involving a signal controller and a power amplifier. A laser sensor is utilized to obtain the actual vibration amplitude for a better comparison.

As any vibration excitation occurs, the AVS network operates accordingly. The mechanical energy will be converted and delivered to the power management module to offer a uniformed DC power to drive the various electronics and signal management modules. The overall energy output capability of capacitor charging and light emitting diode arrays power supply is demonstrated in Figure S7, Supporting Information. For the practical monitored aeolian vibration on overhead transmission lines, it will continuously occur for several hours.[5] In contrast, the AVS unit operates effectively after just a few minutes of vibration excitation, which is enough driven by the aeolian vibrations occurring on the transmission line. Meanwhile, the vibration behaviors reflected by the voltage signals generated from the AVS network will be further processed in the signal processing module. This module can identify the voltage signal as vibration amplitude in real-time. When the current vibration amplitude exceeds the preset value, a warning signal will be transmitted to a mobile phone via Bluetooth module (Figure 6c, Video S1, Supporting Information). In practical use, the sensor signal is wirelessly transmitted to the terminals installed on the tower within a distance of 100 m, and the terminals send the data through the communication base station nearby to mobiles or other receivers. Herein, a self-powered wireless warning system that acts as an overhead transmission line aeolian vibration state online-monitoring is demonstrated, which is helpful for the online-monitoring and state awareness for the transmission line.

Furthermore, a transmission line aeolian vibration mapping system is proposed based on the LabView software platform. In the platform, the signal of each AVS unit is captured by a multichannel operator and delivered to a customized program. The program can calculate the distributed vibration amplitude at any location via the spline interpolation method based on the collected data, based on which the vibration mapping graph of the whole transmission line can be plotted. In addition, the current maximum vibration frequency and amplitude can also be obtained. For any triggered lines, the global detection data can be first analyzed in a rapid manner to evaluate the warning state of the whole line (Figure 6d, Video S2, Supporting Information). Figure 6e demonstrates the operation of the transmission line aeolian vibration mapping system at various amplitudes triggered by the shaker under a fixed frequency. It can be observed that the overall bending degree of the wire becomes higher with the increased amplitude, which will endanger the stability of the wire near the clamp end. The vibration distribution mapping at various frequencies with a fixed amplitude is also displayed in Figure 6f. The maximum amplitude exists at a frequency of 20 Hz, this is because the current value is close to the resonant frequency of the wire, resulting in a higher amplitude due to the resonance phenomenon.[42] Based on the mapping information, the global vibration distribution of the transmission line can be easily visualized, potentially enabling an in-depth wire fatigue damage analysis and health condition evaluation.

In addition, when it comes to practical use in field, the abnormal vibration intensity caused by the standing waves will bring about the unevenness of distribution.[43–45] Therefore, average wind speed at a location during seasons should be statistically collected, and the simulated standing waves will be calculated to obtain the average vibration distributions, which can guide the installation of the network and the weight allocation for each sensor unit. Moreover, the resonance frequency randomly occurring at varied positions caused by the intrinsic frequency behavior of transmission lines should also be considered for ameliorating the accuracy for on-site monitoring. In the normal case, if a frequency perceived by a sensor is different from others, which means there is a resonance occurring at this sensor position, then the credibility will be automatically reduced in the signal proceeding process in software, and a lower weight or even zero weight will be attached to this sensor. While for the extreme situations that each position on the line experience the resonance frequency, the weight alteration strategy would be inapplicable, at this point, more sensors should be widely installed at typical positions to maintain the monitoring accuracy.

The above demonstrations prove the feasibility of the application of the cooperative AVS network for transmission line vibration monitoring. The TENG-based self-powered sensor network can be considered as a low-cost, flexible, and effective method for the large-scale distributed monitoring of any long-span, massive operating equipment, with global, accurate, and rapid results. This also provides a novel perspective to monitor and evaluate the critical lengthy span transmission line condition, and can be further utilized for the damper arrangement and optimization.

3. Conclusion

In summary, a self-powered sensor network constructed by AVS units with a spring-mass based TENG (S-TENG) is proposed and demonstrated for the effective vibration energy harvesting and broadband vibration monitoring facing the application requirements in power grid. The S-TENG is composed of a TENG and a spring-mass combination, in which the TENG is designed into a multi-layered helical structure with the triboelectric layers of PTFE films, forming a contact separation mode for energy harvesting and vibration sensing, simultaneously. The structural parameters of TENG such as vibration space and helical layer numbers were rationally optimized and the device with 30 mm vibration space and 6-layer number exhibits both excellent output performance and broader vibration amplitude response range. The output power for TENG is 2.5 mW at the matched impedance of 5 MΩ, and the amplitude response range of TENG is enhanced into the enlarged range of 0.7–5 mm. The durability and stability performance of TENG has been demonstrated over up to 500k cycles in continuous

ADVANCED
SCIENCE NEWS
www.advancedsciencenews.com

ADVANCED
ENERGY
MATERIALS
www.advenergymat.de

operations, with only 1.9% decrease for the PTFE. Moreover, the spring-mass combinations with customized parameters are further integrated with the TENGs to enhance the frequency response range (5–50 Hz). Meanwhile, the weight factors were assigned according to the individual error rate of each S-TENG, based on which a weight allocation strategy is proposed to improve the accuracy and credibility of the final results. Finally, the S-TENG is connected to the external circuit to form an AVS unit, where the signals produced from the TENG flow into the MCU module through a signal conditioner to assess the potential warning based on the current state, with the warning message being wirelessly transmitted to the terminals installed on the towers (instead of mobile phone in Demo) via Bluetooth module within a transmission distance of 100 m, demonstrating a self-powered wireless warning system for aeolian vibration state online-monitoring. In the demonstration of the transmission line aeolian vibration mapping system, an array of AVS units were distributely deployed on the simulated transmission line, and multi-channels were employed to transmit the signals into the LabView platform, with the visible vibration distribution mapping information for both amplitude and frequency. The proposed TENG-based network provides a highly efficient method for micro-vibration energy harvesting, and more importantly, an innovative strategy for the online vibration distribution monitoring, which diversifies the monitoring methods of overall state-awareness to facing the challenges in power grid sensor network visualization.

4. Experimental Section

Modification of PTFE Film: In order to enhance the surface roughness and triboelectrification, the PTFE films (100 μm in thickness) were placed in an inductively coupled plasma instrument (STS LPX ASE-SR) chamber and etched by 400 W, 40 kHz air plasma for 10 min. After that, the treated samples were ultrasonically cleaned with deionized water and ethanol successively, then dried in a drying oven before use.

Fabrication of S-TENG: The S-TENG mainly consisted of two components: a 6-layered TENG and a spring-mass combination.

For the TENG, a 1 mm thick acrylic sheet was cut by a laser cutter (Universal Laser System PLS6.75) into an open-ended ring (inner diameter of 40 mm, outer diameter of 60 mm). A Cu foil (50 μm in thickness) was attached to the back surface of the acrylic ring as an electrode. A sponge (1 mm in thickness) and a Cu-coated PTFE film were attached to the front surface of the acrylic ring, successively. The above 6 similar acrylic rings were glued to each other at the opening position, forming a helical structure.

For the spring-mass combination, a 5 mm thick acrylic sheet was cut into circular blocks (diameter of 60 mm) to play respectively as a bottom base and a top mass block, and the center of the mass block was cut with a circular hole (diameter of 15 mm). A steel spring (30 mm × 30 mm × 30 mm) was fixed between the two cut circular blocks to form the spring-mass combination. Then the TENG was anchored to connect the top and bottom substrates. An acrylic shaft with dimensions of 15 mm × 15 mm × 60 mm was placed at the center of the bottom base to ensure the stability of the S-TENG in the vertical direction. Finally, a spliced cylinder acrylic box (80 mm × 80 mm × 70 mm) was utilized as the shell of the S-TENG.

Experimental Measurements: For the evaluation of output performance, the TENG was mounted on an electromagnetic shaker (HEV-50) driven by an amplifier (HEA-50) and signal controller (RIGOL DG1022Z) with a sinusoidal signal output, while the current oscillation was monitored by a laser microscopic motion sensor (Panasonic HG-C1100). The typical electrical signals of the TENG were measured by a programmable electrometer (Keithley 6514). For the multichannel measurement, the voltage signals were measured by an ADC (National Instrument NI 9220, 16-channel voltage measurement module, ± 10 V). The measurement signals were visualized in a high-speed data acquisition system under LabView 2016.

System Demonstration: The self-powered wireless warning system was integrated by the S-TENG, a signal controller (Arduino UNO R3), a Bluetooth transmitter (HC-08), a Bluetooth receiver (a mobile phone), and an analysis software for online-monitoring of transmission line aeolian vibration. The transmission line aeolian vibration mapping system was constructed based on the LabView software platform, which enables real-time acquisition data analysis and vibration state visualization.

Supporting Information

Supporting Information is available from the Wiley Online Library or from the author.

Acknowledgements

Conflict of Interest

The authors declare no conflict of interest.

Data Availability Statement

The data that support the findings of this study are available from the corresponding author upon reasonable request.

Keywords

[1] G. Bedi, G. K. Venayagamoorthy, R. Singh, R. R. Brooks, K. Wang, *IEEE Internet Things J.* **2018**, *5*, 847.
[2] Z. L. Wang, *Nano Energy* **2019**, *58*, 669.
[3] S. Yong, J. Wang, L. Yang, H. Wang, H. Luo, R. Liao, Z. L. Wang, *Adv. Energy Mater.* **2021**, *11*, 2101194.
[4] Z. Ren, X. Liang, D. Liu, X. Li, J. Ping, Z. Wang, Z. L. Wang, *Adv. Energy Mater.* **2021**, *11*, 2101116.
[5] B. Godard, S. Guerard, J. Lilien, *IEEE Trans. Power Delivery* **2011**, *26*, 2111.
[6] M. Zhang, J. Xu, G. Zhao, G. Hao, *IET Gener. Transm. Distrib.* **2018**, *12*, 2918.
[7] H. Wang, Y. B. Liu, Y. M. Dong, H. Xu, *Proc. CSEE* **2008**, *28*, 123.
[8] M. L. Lu, J. K. Chan, *IEEE Trans. Power Delivery* **2007**, *22*, 1822.
[9] Y. Qi, X. Rui, K. Ji, C. Liu, C. Zhou, *Adv. Mech. Eng.* **2019**, *11*, 1.

[10] L. Bjerkan, *Appl. Opt.* **2000**, *39*, 554.

[11] Q. Chai, Y. Luo, J. Ren, J. Zhang, J. Yang, L. Yuan, G. Peng, *Opt. Eng.* **2019**, *58*, 072007.

[12] J. M. Ko, Y. Q. Ni, *Eng. Struct.* **2005**, *27*, 1715.

[13] L. Zhao, X. Huang, Y. Zhao, W. Si, *Struct. Control Health Monit.* **2018**, *25*, e2143.

[14] A. Kubba, K. Jiang, *Sensors* **2014**, *14*, 188.

[15] X. Huang, L. Zhao, J. Shu, S. Ji, Y. Zhang, *High Voltage Eng.* **2012**, *38*, 1863.

[16] Y. Chen, Y. Wang, Y. Zhang, H. Zou, Z. Lin, G. Zhang, C. Zou, Z. L. Wang, *Adv. Energy Mater.* **2018**, *8*, 1802159.

[17] F. Fan, Z. Tian, Z. L. Wang, *Nano Energy* **2012**, *1*, 328.

[18] Z. L. Wang, J. Chen, L. Lin, *Energy Environ. Sci.* **2015**, *8*, 2250.

[19] K. Dong, J. Deng, Y. Zi, Y.-C. Wang, C. Xu, H. Zou, W. Ding, Y. Dai, B. Gu, B. Sun, Z. L. Wang, *Adv. Mater.* **2017**, *29*, 1702648.

[20] G. Zhu, Z.-H. Lin, Q. Jing, P. Bai, C. Pan, Y. Yang, Y. Zhou, Z. L. Wang, *Nano Lett.* **2013**, *13*, 847.

[21] J. Wang, Z. Wu, L. Pan, R. Gao, B. Zhang, L. Yang, H. Guo, R. Liao, Z. L. Wang, *ACS Nano* **2019**, *13*, 2587.

[22] B. Zhang, Z. Wu, Z. Lin, H. Guo, F. Chun, W. Yang, Z. L. Wang, *Mater. Today* **2020**, *10*, 031.

[23] H. Yu, X. He, W. Ding, Y. Hu, D. Yang, S. Lu, C. Wu, H. Zou, R. Liu, C. Lu, Z. L. Wang, *Adv. Energy Mater.* **2017**, *7*, 1700565.

[24] J. Shao, T. Jiang, W. Tang, L. Xu, T. W. Kim, C. Wu, X. Chen, B. Chen, T. Xiao, Y. Bai, Z. L. Wang, *Nano Energy* **2018**, *48*, 292.

[25] S. Li, D. Liu, Z. Zhao, L. Zhou, Z. L. Wang, *ACS Nano* **2020**, *14*, 2475.

[26] S. Wang, S. Niu, J. Yang, L. Lin, Z. L. Wang, *ACS Nano* **2014**, *8*, 12004.

[27] C. Deng, W. Tang, L. Liu, B. Chen, M. Li, Z. L. Wang, *Adv. Funct. Mater.* **2018**, *28*, 1801606.

[28] J. Wang, L. Pan, H. Guo, B. Zhang, R. Zhang, Z. Wu, C. Wu, L. Yang, R. Liao, Z. L. Wang, *Adv. Energy Mater.* **2019**, *9*, 1802892.

[29] G. Zhu, P. Bai, J. Chen, Z. L. Wang, *Nano Energy* **2013**, *2*, 688.

[30] M. Xu, P. Wang, Y.-C. Wang, S. L. Zhang, A. C. Wang, C. Zhang, Z. Wang, X. Pan, Z. L. Wang, *Adv. Energy Mater.* **2018**, *8*, 1702432.

[31] C. Wu, R. Liu, J. Wang, Y. Zi, L. Lin, Z. L. Wang, *Nano Energy* **2017**, *32*, 287.

[32] J. Chen, G. Zhu, W. Yang, Q. Jing, P. Bai, Y. Yang, T.-C. Hou, Z. L. Wang, *Adv. Mater.* **2013**, *25*, 6094.

[33] X. Wang, S. Niu, Y. Fang, Y. Yin, C. Hao, K. Dai, Y. Zhang, Y. Zheng, Z. L. Wang, *ACS Nano* **2017**, *11*, 1728.

[34] S. Niu, S. Wang, L. Lin, Y. Liu, Y. S. Zhou, Y. Hu, Z. L. Wang, *Energy Environ. Sci.* **2013**, *6*, 3576.

[35] R. D. I. G. Dharmasena, K. D. G. I. Jayawardena, C. A. Mills, J. H. B. Deane, J. V. Anguita, R. A. Dorey, S. R. P. Silva, *Energy Environ. Sci.* **2017**, *10*, 1801.

[36] J. Peng, S. D. Kang, G. J. Snyder, *Sci. Adv.* **2017**, *12*, eaap8576.

[37] D. K. Davies, *J. Phys. D: Appl. Phys.* **1969**, *2*, 1533.

[38] Z. L. Wang, *ACS Nano* **2013**, *7*, 9533.

[39] L. Bjerkan, O. Lillevik, *Cigre Session* **2004**, *2*, 314.

[40] C. B. Williams, R. B. Yates, *Sens. Actuators, A* **1996**, *52*, 8.

[41] M. Ervik, *IEEE Trans. Power Appar. Syst.* **1981**, *100*, 2149.

[42] F. Wang, Y. Wang, R. Zhou, C. Chen, *J. Chongqing Univ.* **2018**, *41*, 42.

[43] W. Yin, L. Lin, *Nonlinear Eng.* **2021**, *10*, 395.

[44] M. Kraus, P. Hagedorn, *IEEE Trans. Power Delivery* **1991**, *6*, 1264.

[45] R. Whapham, *Electr. Transm. Subst. Struct. Conf.* **2014**, *1*, 262.